Efficient 6 GHz Wi-Fi based Occupancy Detection: Channel Model-Informed Feature Engineering and Random Forest Optimization

Zeyang Li, Jie Zhang, *Member, IEEE,* Claudio R. C. M. Da Silva, Okan Yurduseven, *Senior Member, IEEE,* Trung Q. Duong, *Fellow, IEEE,* Carlo Fischione, *Fellow, IEEE,* and Simon L. Cotton, *Fellow, IEEE*

***Abstract*—This paper investigates the use of the newly opened, and relatively unexplored, 6 GHz band for office occupancy detection using Wi-Fi sensing. To deliver accurate and efficient occupancy detection, we develop a novel channel model-informed feature engineering method combined with a random forest optimization strategy. Specifically, physically interpretable channel state information (CSI) amplitude-based features, such as the Rician K-factor and channel coherence time, are employed to capture channel variations induced by human presence and movement. A dual sliding window approach is introduced to effectively extract temporally relevant channel parameters, significantly improving computational efficiency and classification accuracy. Experimental validation conducted in a realistic office environment demonstrates that the proposed method achieves an average occupancy classification accuracy of 98.28%, outperforming existing methods while substantially reducing computational complexity. These findings suggest that integrating this Wi-Fi sensing approach into next-generation networks (e.g., IEEE 802.11bf) can enhance real-time responsiveness and reliability in smart building applications such as security and energy management.**

***Index Terms*—6 GHz band, channel state information, feature extraction, office occupancy detection, random forest, Wi-Fi sensing.**

I. Introduction

Wi-Fi sensing has rapidly emerged as a promising technology for passive indoor monitoring, enabling applications such as occupancy detection, localization, and activity recognition [1]–[4]. The introduction of the IEEE 802.11bf standard [5] and the availability of the 6 GHz unlicensed band provide the opportunity for higher spatial resolution, improved sensing accuracy, and reduced interference [6]—making Wi-Fi particularly attractive for smart building systems that aim to optimize energy efficiency, ensure occupant safety, and improve space utilization [7]–[9].

Previous studies have explored a range of Wi-Fi sensing techniques. Deep learning approaches such as convolutional neural network (CNN), long short-term memory (LSTM), and hybrid models have demonstrated high performance in activity recognition and gesture sensing tasks [1], [10], [11], but are computationally expensive and difficult to scale. Conventional classifiers like Random Forests have also been applied for feature selection and classification [12], yet they typically rely on raw or engineered features without physical grounding. Moreover, few works incorporate channel model-based parameters—such as the Rician K-factor, channel coherence time (CCT), or average fade duration (AFD)—that are sensitive to environmental dynamics and can be leveraged for efficient and interpretable sensing.

In this paper, we propose a physically-informed and computationally efficient Wi-Fi sensing framework for real-time office occupancy detection in the 6 GHz band. Our approach uses a dual sliding window to extract physically interpretable features from CSI amplitude data, including the Rician K-factor, CCT, AFD and level crossing rate (LCR). These features are then processed through an optimized random forest-based feature selection and classification pipeline that achieves high accuracy with minimal latency.

A. Related Works

Recent research has highlighted the effectiveness of Wi-Fi sensing for indoor activity recognition and localization. Zhang et al. [1] utilized CSI amplitude and phase data to recognize in-the-air handwriting gestures, introducing domain-independent features such as Dynamic Phase Vector (DPV) and Motion Rotation Variable (MRV), achieving robust performance across varying device placements. In localization, Ding et al. [13] proposed a 5 GHz Wi-Fi-based system combining t-SNE optimization with a recurrent neural network (RNN) model, achieving sub-meter mean error in laboratory environments. Other works have also demonstrated improvements in indoor positioning using CSI-based learning frameworks [14]–[17].

Wi-Fi-based device-free occupancy sensing has attracted substantial attention due to its non-intrusiveness and ubiquity in smart environments. Wang *et al.* [18] introduced CARM, a CSI amplitude-based system leveraging principle component analysis (PCA), discrete wavelet transform (DWT), and hidden markov model (HMM) to achieve 96% accuracy, yet struggled with concurrent multi-user detection. Yang *et al.* [19] employed matrix decomposition for real-time CSI analysis in smart homes, showing high accuracy but similar scalability limitations. Liu *et al.* [20] developed Wi-PSG, utilizing synthetic subcarriers and hybrid time-frequency features to detect rhythmic movement disorders with over 97% accuracy. Recent works [21], [22] further explored self-adaptive occupancy detection. Specifically, WiSOM [21] introduced a DBSCAN-control chart pipeline with DWT filtering and PCA features,

This work was funded in part by Project REASON, a UK Government funded project under the Future Open Networks Research Challenge (FONRC) sponsored by the Department of Science Innovation and Technology (DSIT), and by the UK Engineering and Physical Sciences Research Council (EPSRC) through the EPSRC Hub on All Spectrum Connectivity (EP/X040569/1 and EP/Y037197/1). It was also supported by the SSF SAICOM project.

Z. Li and C. Fischione are with the School of Electrical Engineering and Computer Science, and the Digital Futures, KTH Royal Institute of Technology, 114 28 Stockholm, Sweden. (e-mail: zeyangl, carlofi@kth.se).

J. Zhang, O. Yurduseven and S. L. Cotton are with the Centre for Wireless Innovation (CWI), School of Electronics, Electrical Engineering and Computer Science, Queen's University Belfast, Belfast, BT3 9DT, UK. (e-mail: jie.zhang, okan.yurduseven, simon.cotton@qub.ac.uk).

C. R. C. M. Da Silva is with MediaTek, San Jose, CA, USA. (e-mail: claudio.dasilva@mediatek.com).

T. Q. Duong is with the Faculty of Engineering and Applied Science, Memorial University, St. John's, NL A1C 5S7, Canada and is also with the CWI, School of Electronics, Electrical Engineering and Computer Science, Queen's University Belfast, Belfast, BT3 9DT, UK. (E-mail: tduong@mun.ca).

achieving over 98% detection accuracy while addressing multipath effects, intensity variation of daily activities, and non-line of sight (NLoS) propagation. A similar framework was also validated in [22], showing high resilience to temporal CSI drift and daily activity instance imbalance using auto-tuned DBSCAN and real-time threshold updates. Zeleny et al. [23] introduced a Wi-Fi probe request-based method using deep learning models, which achieved up to 91.8% accuracy in presence detection. Meanwhile, random forest classifiers have shown strong performance in CSI-based feature selection and noise robustness [12], motivating our adoption of a physics-aware feature set and tree-based classification for efficient and interpretable occupancy inference.

Recent efforts have advanced CSI amplitude-based sensing for activity and occupancy recognition [10], [11], [24], [25]. Zhuravchak et al. [10] compared InceptionTime and LSTM models for classifying seven human activities using sanitized CSI data at 2.4/5 GHz, achieving 61% accuracy. Lin et al. [11] proposed a CNN-based method using smartphone-collected CSI at 5.805 GHz to classify 20 activities, achieving 97.25% accuracy, outperforming LSTM and decision trees. While deep learning models offer high accuracy, they often require significant computational resources and struggle with multi-user environments and generalization across settings.

Other notable contributions in Wi-Fi sensing include the use of temporal and frequency domain analysis for feature extraction. Lee et al. [26] applied short-time Fourier transform (STFT) to CSI amplitude data and used a hybrid CNN-LSTM model for classifying activities such as cooking and sleeping across multiple indoor environments, achieving over 96% accuracy. However, performance was sensitive to receiver placement and multi-user scenarios. Kianoush et al. [27] utilized MIMO-OFDM CSI at 5 GHz with PCA and subspace methods for device-free localization, demonstrating enhanced spatial resolution and reliable multi-target detection using spatial-frequency correlations.

Wi-Fi sensing has also been applied to healthcare and smart home scenarios [28]–[30]. Zein et al. [28] proposed a 5 GHz CSI-based CNN system for real-time fall detection, achieving 95% accuracy with time series augmentation. Yu et al. [29] used CSI amplitude ratios with PCA and deep learning for sleep stage classification over 19 nights, attaining 81.8% accuracy—comparable to radar-based systems but using commodity Wi-Fi devices.

To improve robustness across environments, recent studies have applied transfer learning and adversarial defense in Wi-Fi sensing. Qi et al. [31] introduced a federated transfer learning framework for gesture recognition that preserves privacy and reduces communication cost, achieving high cross-environment accuracy. Wang et al. [32] employed domain generalization and few-shot learning to enhance adaptability with minimal data. Yang et al. [33] proposed a defense framework that improves activity recognition robustness against adversarial perturbations, including Gaussian and bimodal noise.

B. Contribution

Despite recent advances, existing Wi-Fi sensing solutions typically employ computationally intensive deep learning methods, limiting their practical use in real-time occupancy detection. Moreover, many existing Wi-Fi sensing solutions do not make use of physically interpretable channel parameters such as the Rician K-factor and CCT which can be useful for providing deeper insights into the sensing problem. In addition to this, to the best of our knowledge, no such studies investigating occupancy detection in the recently opened 6 GHz band used by Wi-Fi 6E (IEEE 802.11ax) and above have been reported in the open literature. In this work, we address a key challenge in smart office environments: how to achieve fast, reliable, and scalable occupancy detection using Wi-Fi devices in the 6 GHz band. To overcome this challenge, we conduct measurements in a dynamic office environment where multiple people are involved, propose a lightweight, physically interpretable method that utilizes CSI amplitude data to extract meaningful features inspired by wireless channel models. The contributions of this study are as follows:

- We conduct measurements in a real office environment at sub-7 GHz frequencies, aligned with several emerging IEEE 802.11 standards (e.g., IEEE 802.11be [34], IEEE 802.11bf [5], IEEE 802.11bn [35]). Our statistical analysis of key features extracted from the measured channels offers valuable insights into the behavior of sub-7 GHz wireless channels in dynamic office environments.
- We develop a novel dual sliding window approach that effectively extracts temporally relevant, physically interpretable CSI amplitude-based features, such as the Rician K-factor, CCT, and LCR, enabling robust occupancy detection.
- We propose a random forest-based algorithm specifically optimized for channel model-based feature selection, achieving superior classification accuracy and minimal computational overhead suitable for near-real-time applications.
- Extensive experiments conducted in realistic office environments demonstrate the method's effectiveness, achieving 98.28% accuracy and significantly outperforming existing solutions in dynamic scenarios involving multiple occupants.

The rest of the paper is organized as follows. Section II describes the proposed feature extraction and selection methodology. Section III details the experimental setup and methods used to collect CSI amplitude data in the office environment, while Section IV presents an evaluation of our results. Finally, Section V concludes the paper and summarizes key findings.

II. Feature Extraction and Selection

This section presents a CSI amplitude-based approach for office occupancy detection. We first outline the acquisition and interpretation of CSI amplitude, followed by the application of dual sliding windows to extract meaningful features. These features, including channel-specific parameters, are used to construct a random forest classifier. We also detail the feature selection and decision tree optimization processes that enhance classification accuracy and efficiency.

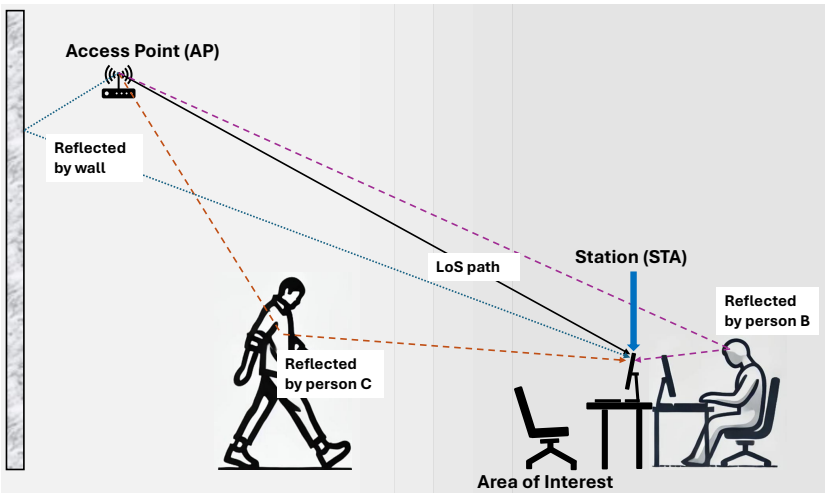

(a) Unoccupied area of interest: the AP–STA link includes a LoS path and a static wall reflection, while people B and C moving outside the target area create additional dynamic paths.

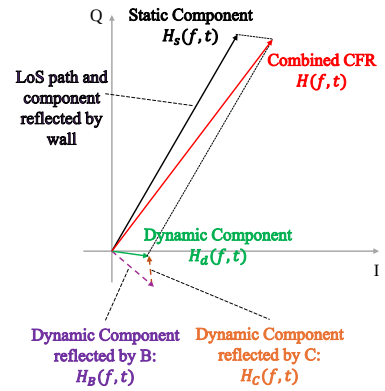

(b) Unoccupied phasor view: channel frequency response $H(f,t) = H_s(f) + H_d(f,t)$; H_s aggregates the LoS and static wall components, and H_B, H_C are dynamic components from B and C. The red vector is the combined CFR.

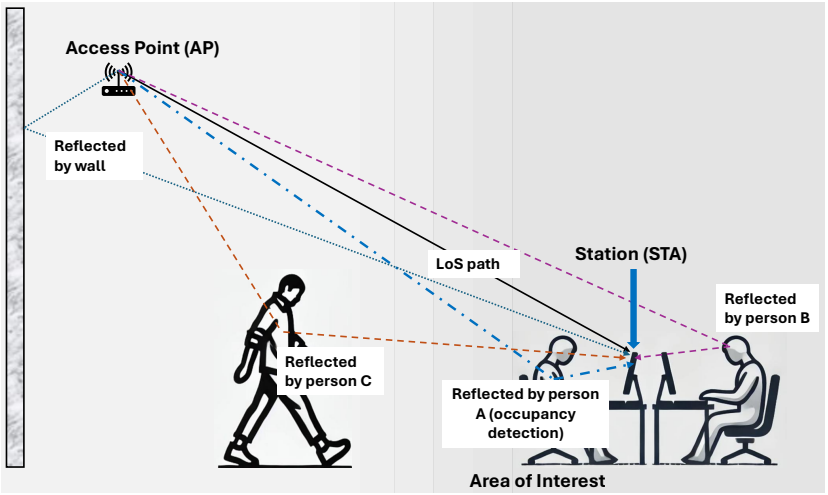

(c) Occupied area of interest: a seated person A within the target area introduces an extra dynamic path $H_A(f,t)$ that perturbs the AP–STA link.

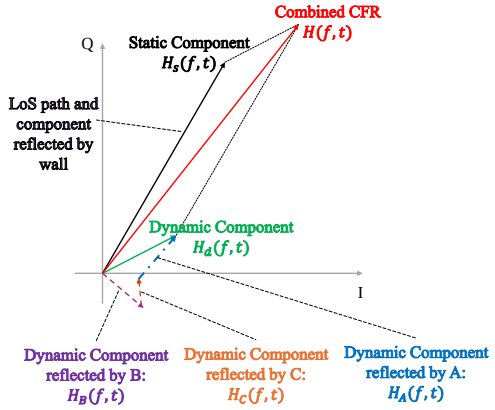

(d) Occupied phasor view: the added component H_A changes the combined CFR.

Fig. 1: Multi-paths in the office and its phasor model.

A. Channel response decomposition

When a wide-band radio signal travels from a transmitter to a receiver it reaches the receiver along L distinct propagation paths—line-of-sight (LoS), wall reflections, edge diffractions, and scatterings. Each path imposes its own delay $\tau_i(t)$ and complex attenuation $a_i(f,t)$, so the frequency response observed at carrier frequency f and time t is the coherent sum

$$H(f,t) = \sum_{i=1}^{L} a_i(f,t)\, e^{-j2\pi f\, \tau_i(t)}. \tag{1}$$

Static versus dynamic multipath: In an office, many paths are immutable (e.g. LoS and wall bounces) while others fluctuate as people move. As illustrated in Fig. 1, we therefore split

$$H(f,t) = H_{\mathrm{s}}(f) + H_{\mathrm{d}}(f,t),$$

with

$$H_{\mathrm{s}}(f) = \sum_{i=1}^{L_{\mathrm{s}}} a_i(f)\, e^{-j2\pi f\, \tau_i}, \qquad \text{(static paths)} \tag{2a}$$

$$H_{\mathrm{d}}(f,t) = \sum_{k=1}^{L_{\mathrm{d}}} a_k(f,t)\, e^{-j2\pi f\, \tau_k(t)}, \quad \text{(dynamic paths)} \tag{2b}$$

where $L = L_{\mathrm{s}} + L_{\mathrm{d}}$. Note that even the LoS component migrates into $H_{\mathrm{d}}(f,t)$ if it is intermittently blocked by a person.

Relating dynamics to occupancy: For device-free occupancy sensing we refine the dynamic term:

$$H_{\mathrm{d}}(f,t) = \underbrace{H_{\mathrm{d}i}(f,t)}_{\text{inside target area}} + \underbrace{H_{\mathrm{d}r}(f,t)}_{\text{outside target area}}.$$

TABLE I: Important Symbols used in Section II-B

Symbol	Meaning
T_{d}	CSI sampling interval (seconds)
N_C	Width of CSI-amplitude window (samples)
N_{s}	Step of CSI window / stride between features (samples)
N_F	Width of feature window (features)
m, m'	Index of 1st- and 2nd-level feature types

Hence

$$\textbf{Unoccupied:} \quad H_{\mathrm{u}}(f,t) = H_{\mathrm{s}}(f) \; + \; H_{\mathrm{d}r}(f,t), \tag{3}$$

$$\textbf{Occupied:} \quad H_{\mathrm{o}}(f,t) = H_{\mathrm{u}}(f,t) \; + \; H_{\mathrm{d}i}(f,t). \tag{4}$$

Occupancy detection is therefore a hypothesis test for the presence of the extra term $H_{\mathrm{d}i}(f,t)$: detect $H_{\mathrm{o}}(f,t)$ versus $H_{\mathrm{u}}(f,t)$ using the measured $H(f,t)$. $H_{\mathrm{s}}(f)$ forms a slowly varying baseline. $H_{\mathrm{d}r}(f,t)$ captures background activity outside the region of interest. Only $H_{\mathrm{d}i}(f,t)$ encodes the human-induced perturbations we care about, making it the principal discriminative feature for occupancy classification.

B. Sliding windows, feature extraction, and labelling

Occupancy detection needs to distinguish $H_{\mathrm{o}}(f,t)$ from $H_{\mathrm{u}}(f,t)$. To achieve this, we need to extract features from $H(f,t)$ that can effectively highlight the differences between $H_{\mathrm{o}}(f,t)$ and $H_{\mathrm{u}}(f,t)$. Firstly, we adopt a dual sliding window approach applied across the CSI amplitude. The time interval of signal data sampling is denoted by T_{d}. The important symbols used in this section are summarized in TABLE I.

Step 1 – CSI-amplitude window: From the raw channel response magnitudes $|H(f,t)|$, collect N_C successive samples

$$\mathbb{H}(f;t_1) \; = \; [|H(f,t_1)|, \ldots, |H(f,t_1+(N_C-1)T_{\mathrm{d}})|]. \tag{5}$$

Normalise each amplitude to remove slow fading:

$$\hat{H}(f,t_1+nT_{\mathrm{d}}) = \frac{|H(f,t_1+nT_{\mathrm{d}})|}{\sqrt{\frac{1}{N_C}\sum_{k=0}^{N_C-1}|H(f,t_1+kT_{\mathrm{d}})|^2}}, \tag{6}$$

where $0 \le n < N_C$. Apply a first-level statistic or transform m to obtain a scalar feature

$$R_m(f,t_1) \; = \; \mathcal{F}_m(\hat{H}(f,t_1), \ldots, \hat{H}(f,t_1+(N_C-1)T_{\mathrm{d}})). \tag{7}$$

Advance the CSI window by N_{s} samples ($t_1 \to t_1 + N_{\mathrm{s}}T_{\mathrm{d}}$) and repeat to create a time series of R_m values.

Step 2 – Feature window: To expand the range of features available for analysis, a feature window of size N_{F} is applied on the feature set extracted from the CSI amplitude window. Stack N_F consecutive first-level features into a feature window

$$[R_m(f,t_1),\; R_m(f,t_1{+}N_{\mathrm{s}}T_{\mathrm{d}}), \ldots, R_m(f,t_1{+}(N_F{-}1)N_{\mathrm{s}}T_{\mathrm{d}})]$$

and compute a second-level statistic m':

$$S_{m'}(f,t_1) = \mathcal{G}_{m'}(R_m(f,t_1), \ldots, R_m(f,t_1{+}(N_F{-}1)N_{\mathrm{s}}T_{\mathrm{d}})). \tag{8}$$

Step 3 – Supervised labelling: Labels are assigned to each extracted feature value for use by the classifier in a supervised learning framework. The assignment of a label to a feature value is based on the timestamp of the last data point in the window from which the feature value is extracted. For example, assign to $S_{m'}(f,t_1)$ the occupancy state observed at the timestamp of its last underlying CSI sample,

$$t_{\mathrm{label}} = t_1 + (N_F-1)N_{\mathrm{s}}T_{\mathrm{d}} + (N_C-1)T_{\mathrm{d}}$$

If the region of interest is occupied at t_{label}, label the feature occupied; otherwise label it unoccupied. These labelled features form the input–target pairs for the classifier.

This dual-window pipeline decouples short-term channel fluctuations (captured by R_m) from longer-term occupancy cues (captured by R_m and $S_{m'}$), while the final label synchronises each sample with ground-truth presence data.

C. The Type of Features

In this subsection, we introduce the types of features considered in this paper. Given that channel model parameters offer insights into nature of the signal propagation and hence the environment, we extract these parameters from each CSI amplitude window to use as features.

Considering the propagation geometry depicted in Fig. 1 and discussed above, we consider that the signal transmitted from the access point (AP) to the stations (STAs) undergoes Rician fading [36], [37]. The probability density function (PDF) of the Rician distribution is as follows:

$$f(x) = \frac{x}{\sigma^2}\exp\left(-\frac{x^2+\delta^2}{2\sigma^2}\right) I_0\left(\frac{x\delta}{\sigma^2}\right), \tag{9}$$

where x is the envelope of the small-scale fading and $x \ge 0$, $I_0(\cdot)$ is the 0th order modified Bessel function of the first kind. A useful parameter associated with Rician fading is the Rician K factor, $K = \frac{\delta^2}{2\sigma^2}$, which quantifies the ratio of the power of the direct LoS signal to the total power of all other multipath components. Similarly, the root mean square (rms) signal power in a Rician fading channel can be defined as $\Omega' = \delta^2 + 2\sigma^2$, which is the total power received via the direct and multipath components. In this paper, we extract the Rician δ^2, $2\sigma^2$, and K parameters and use these as channel model-based features. Specifically, for each CSI amplitude window, Rician channel parameters are estimated by applying maximum likelihood estimation (MLE) on all signal amplitudes within the window. The Rician channel parameters extracted from the windows become random variables. Other features extracted from the CSI amplitude window include: mean and the standard deviation (STD) of the amplitudes within the window, peak to average ratio (PAR), CCT, AFD, and LCR.

Channel parameters extracted from CSI amplitude windows provide a compact yet powerful representation of channel dynamics. These parameters directly reflect physical propagation characteristics, making the system inherently robust to noise and less sensitive to irrelevant variations. Moreover, extracting features based on known fading distributions greatly reduces the complexity of the system compared to deep-learning-based feature extraction techniques, thereby enabling near real-time occupancy detection.

Once the Rician channel parameters are extracted from the CSI amplitude, feature windows, as described in Subsection

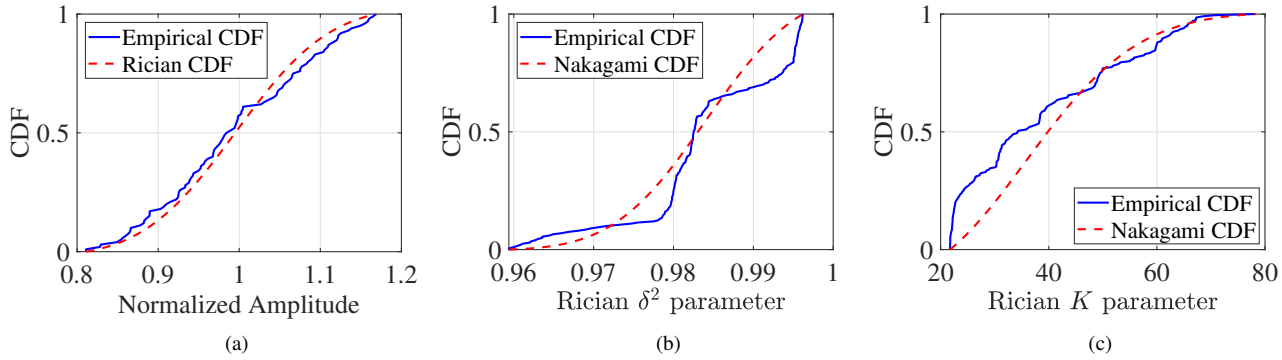

(a) (b) (c)

Fig. 2: CDFs of: (a) Rician distribution with parameters δ^2, $2\sigma^2$, and K, extracted from a CSI amplitude window using MLE and fitted to the empirical data of the same window; (b) Nakagami-m distribution with parameters m and Ω, extracted from a feature window of the Rician δ^2 parameter using MLE, and fitted to the empirical data of the feature window; (c) Nakagami-m distribution with parameters m and Ω, extracted from a feature window of the Rician K parameter using MLE, and fitted to the empirical data of the feature window.

II-B, are applied to the vectors of the Rician parameters. To characterize the shape of the PDF of the Rician δ^2, $2\sigma^2$, and K parameters obtained from each CSI amplitude window, the Nakagami-m distribution [38], [39] is employed. The PDF of the Nakagami-m distribution is given by:

$$f(z) = \frac{2m^m}{\Gamma(m)\Omega^m} z^{2m-1} \exp\left(-\frac{m}{\Omega} z^2\right), \tag{10}$$

where $z \geq 0$, $m \geq 1/2$ and $\Omega > 0$. The parameters m and Ω are extracted from each feature window using MLE. Fig. 2 (a) shows an example of the Rician distribution fitted to some of the normalized CSI amplitude data obtained for window 1 of Scenario 1. As we can see, it provides an excellent fit to the empirical data. Figs. 2(b) and 2(c) show examples of the Nakagami-m distribution fits to δ^2 and K obtained for window 1 in Scenario 3. For these examples, the Nakagami-m distribution is shown to provide an adequate fit to both[1]. Although the Nakagami-m distribution is not used to directly extract features, it provides a flexible and generalizable statistical model for characterizing the temporal variability of the extracted Rician parameters (δ^2, K), which contributes to the robustness of the system across diverse fading scenarios.

It is also worth noting that Rayleigh fading is a special case of Rician fading when the K-factor approaches zero, which allows our framework to accommodate both LoS and NLoS scenarios. Additionally, we also note that the Rician distribution can be used to approximate the Nakagami-m distribution [40]. While more complex fading models (e.g., κ-μ [41], κ-μ / inverse gamma [42] or other shadowed κ-μ fading models [43] etc.) could be used to extract additional features, they would significantly increase the computational cost of the feature extraction process, making them less suitable for real-time deployment.

To obtain additional insights from the signal amplitude, we also analyze the AFD and LCR from the feature windows applied on these extracted Rician δ^2, $2\sigma^2$ and K parameters, and all other features from the CSI amplitude windows. For example, as shown in Fig. 3, the Rician K parameter is derived from the CSI amplitude window. Then, by applying a threshold (depicted as the red line in the normalized Rician K plot) to the normalized Rician K parameter, both AFD and LCR are obtained from the feature window. The time interval between two consecutive amplitude data points is 4 milliseconds in Fig. 3 (a). The CSI amplitude window was set to a size of $N_{\mathrm{C}} = 100$, while the feature window was sized at $N_{\mathrm{F}} = 8$. Additionally, the CSI amplitude window used a step size of $N_{\mathrm{s}} = 30$.

D. Feature Selection and Classification

A random forest-based algorithm is employed to select critical features from the feature lists described in subsection II-C, as random forests can handle numerous input variables and identify the most important ones. Initially, κ_{a} decision trees are generated using the features from the feature lists to perform the classification task of determining whether the area of interest is occupied or unoccupied. These decision trees are ranked based on their classification accuracy, and the top κ_{t} decision trees with the highest accuracy are selected ($\kappa_{\mathrm{t}} \ll \kappa_{\mathrm{a}}$). The features chosen by these top κ_{t} trees are then used to generate a new set of κ_{a} decision trees. Once again, the κ_{t} trees with the highest accuracy are selected from these new trees, and their selected features are used to create another round of κ_{a} new decision trees. This process is repeated, and with each cycle, the number of features selected by the κ_{t} trees decreases. The cycle continues, provided the accuracy remains above a certain threshold T_{acc}, until there is a minimal reduction in the number of features within the κ_{t} decision trees. Fig. 4 provides an overview of the feature selection process. In this paper, we define T_{acc} as $0.8\times$ the classification accuracy achieved by κ_{a} decision trees using all features, without any feature selection. In addition, $T_{\mathrm{nf}} = 0$.

Our classification framework is based on supervised learning, where labeled CSI amplitude samples are used to train

[1]A description of the data collected in different Scenario is given in Section III

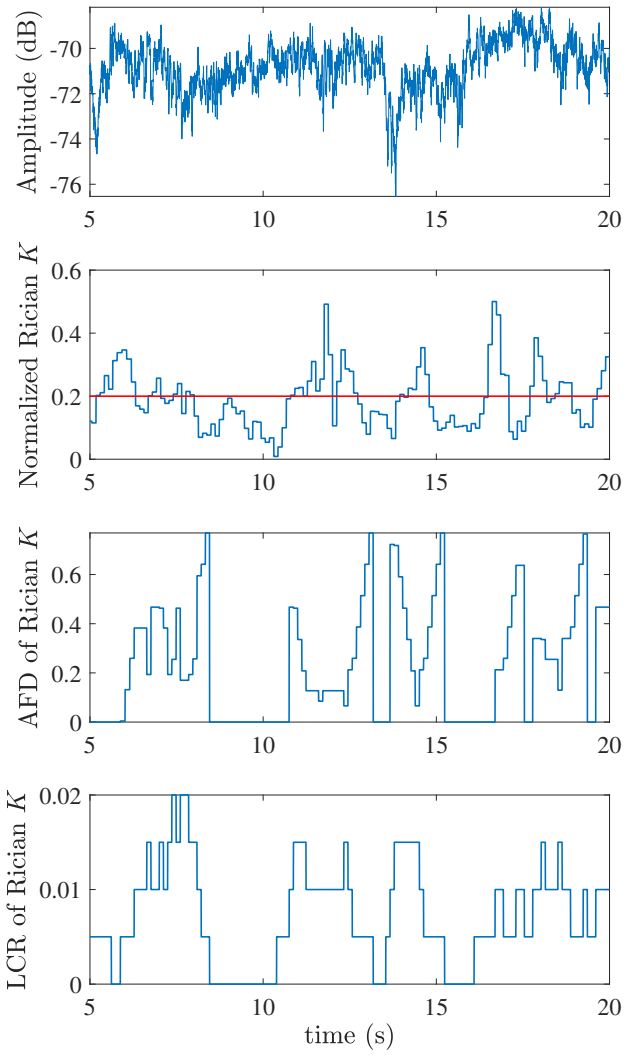

Fig. 3: Rician K parameters extracted from the CSI amplitude windows, AFD and LCR extracted from the feature windows applied on the normalized Rician K parameters.

a random forest classifier to distinguish between occupied and unoccupied scenarios. Compared to deep learning methods, our random forest-based approach maintains low model complexity while offering competitive accuracy. The decision trees used in the classifier are shallow and interpretable, and the iterative feature selection process further reduces input dimensionality to optimize both speed and performance.

E. Classifier Training for Multiple Wireless Links

The process of office occupancy classification, utilizing wireless links between an AP and multiple STAs as input, is shown in Fig. 5. Specifically, during the offline training phase illustrated in Fig. 5 (a), features are initially extracted from each wireless link. Subsequently, feature selection is

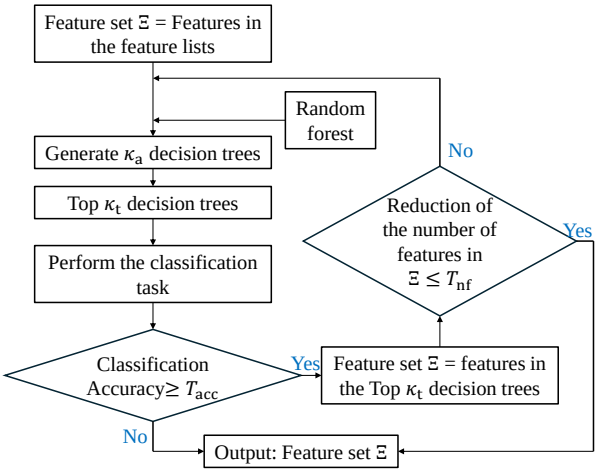

Fig. 4: The flowchart of feature selection.

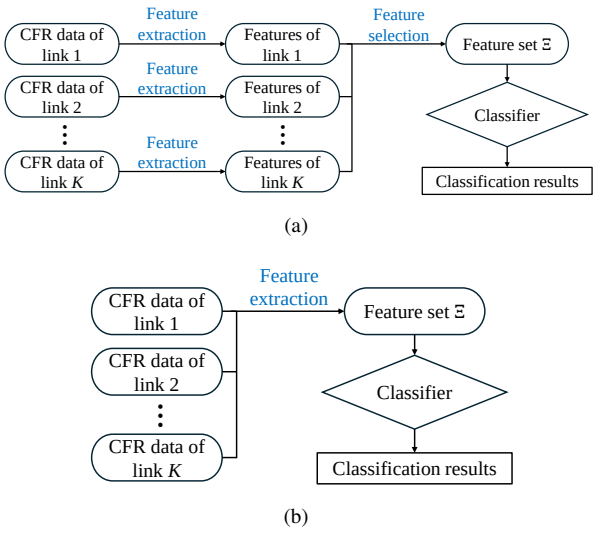

Fig. 5: Flowcharts of (a) offline training phase; and (b) online classification phase for multiple wireless links.

conducted on the complete set of extracted features, forming the selected feature set denoted as Ξ. This feature set Ξ then serves as the input for training the classifier. In the online classification phase, shown in Fig. 5 (b), only the features within the designated set Ξ are extracted from the wireless links. The trained classifier then utilizes these extracted features to determine occupancy status.

III. Measurement Setup, Environment and Procedure

The following section details the methodology employed for collecting the CSI amplitude data related to office occupancy. It outlines the experimental setup, measurement environment, and the specific scenarios considered to ensure the reliability and accuracy of the collected data.

A. Measurement Environment

The channel measurements for office occupancy were conducted in an indoor office situated on the first floor of the

Fig. 6: Measurement Environment: the office used for data collection showing one AP and four STAs (STA1–STA4). The AP is mounted near the ceiling, and the STAs are placed on monitors at four desks.

three-story QTQ building at Queen's University Belfast, UK. The measurement environment is depicted in Fig. 7. The office consisted of three boundary walls constructed from gypsum plasterboard mounted on metal studs, while the fourth wall was made of glass. The floor was covered with polypropylene-fiber, rubber-backed carpet tiles, and the metal ceiling was fitted with mineral fiber tiles supported by two metal columns extending from the floor, which were part of the building's structural design. The ceiling height was 2.70 m above the ground. The office space also contained various furnishings, including eight desks, each equipped with a chair and a computer, as shown in Fig. 6.

B. Measurement Setup

In this study, experiments were conducted using a compact Keysight P5005B Streamline Vector Network Analyzer (VNA) with two ports. One port was connected to a single antenna acting as the transmitter (representing the AP), while the other port was connected to an RF switch with four antennas, using low-loss, phase-matched flexible coaxial cables. The antennas used in the experiments were all omnidirectional 6.5 GHz AntennaWare BodyWave ultra-wideband (UWB) antennas, with a consistent omnidirectional gain of +3 dBi [44]. The antennas exhibited a -10 dB bandwidth ranging from 6.2 to 7.1 GHz. The VNA was connected to a laptop via an active fiber optic cable, facilitating remote control of the device. Two positions of the transmitter antenna (or equivalent AP) were investigated: one at the center of the office room (Fig. 7 (a)) and the other near one of the walls (Fig. 7 (b)). In both configurations, the antenna height was maintained at 2.60 meters above the ground. Each receiver antenna was mounted on a monitor at the desks, as shown in Fig. 6. The study focused on a frequency of 6.425 GHz. During the experiments, repetitive sweeps were performed across the four receiver antennas, recording forward path gain (i.e., S_{21}), representing the

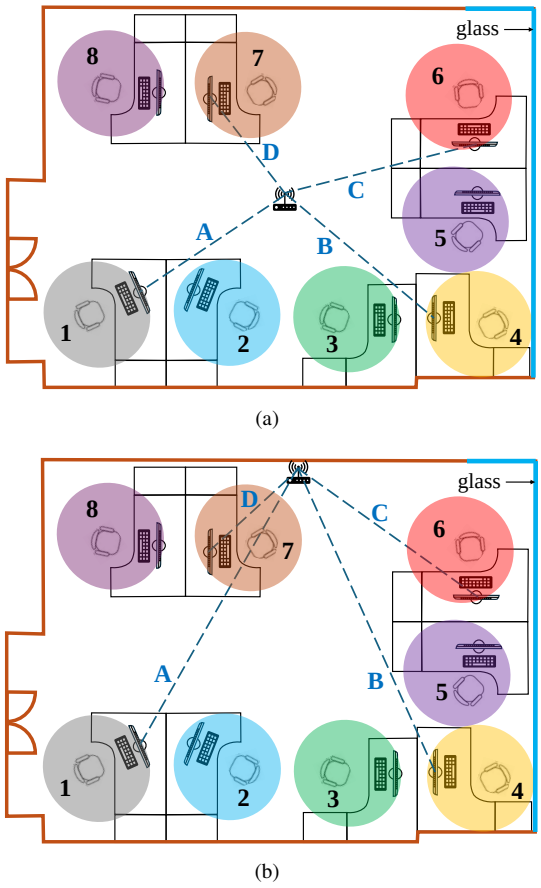

Fig. 7: Considered scenarios: (a) AP position I: the transmitter is located at the center ceiling of the office; (b) AP position II: the transmitter is located at one of the walls of the office.

complex signal, with an intermediate frequency (IF) bandwidth of 100 kHz. The amplitude was obtained from the complex signal by computing its magnitude. For each experimental session, a minimum of 15,000 sweeps across different wireless links were conducted. Each sweep, including the data logging period, lasted roughly 4 milliseconds and captured complex signal data from each link.

C. Measurement Procedure

The experiments were conducted with four adult male participants. The participants alternately occupied designated areas around each office desk. To simulate realistic workplace conditions, three individuals were seated in adjacent areas while a fourth individual walked around the room, introducing time-varying channel conditions to the wireless links. The walking pattern was random from one trial to another. The office occupancy settings analyzed in this study are presented in Table II. For instance, in occupancy setting 1, areas 1, 2, and 3 are occupied, while all other areas remain unoccupied. Each occupancy setting was tested in two separate trials, with each trial lasting 60 seconds. Given the presence of two distinct AP locations and eight different occupancy settings, this results in a total of 16 unique scenarios. Figure 8 illustrates examples of the measured signal amplitudes over time for different

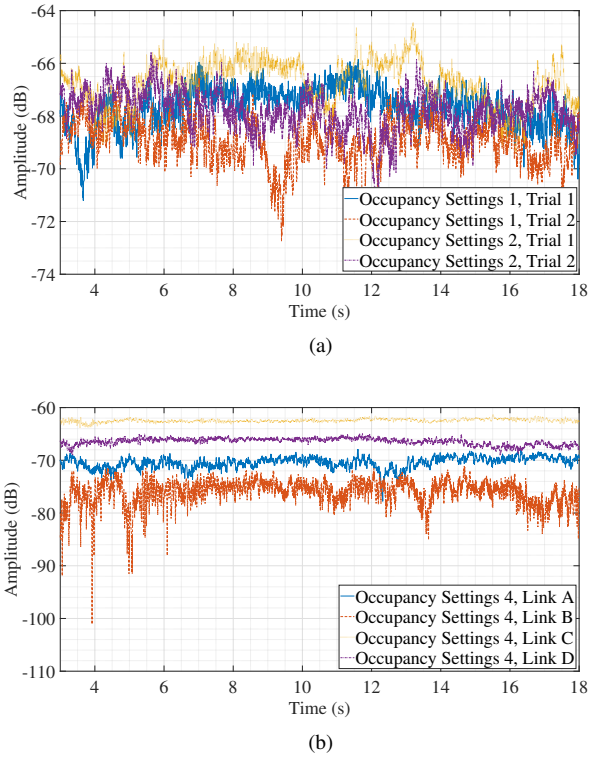

Fig. 8: Amplitude of the signal across time in AP position II: (a) Amplitude of the signal of link C in occupancy setting 1 and 2; (b) Amplitude of the signal of link A, B, C and D in occupancy setting 4.

occupancy settings and trials in AP position II. In Figure 8(a), the amplitude of link C is shown for occupancy settings 1 and 2. Because occupied areas 1, 2, 3, and 4 lie relatively far from link C, the main source of disturbance for this link is the individual walking around the room. Figure 8(b) displays the amplitudes of links A, B, C, and D in occupancy setting 4. Here, links C and D exhibit higher amplitudes than links A and B, likely because they are shorter. Conversely, link B experiences the greatest disturbance, as it is situated closest to the occupied areas.

IV. Performance Evaluation

This section begins with a statistical analysis of the key channel parameters that influence the accuracy and reliability of office occupancy detection. Moreover, we evaluate the performance of the top $\kappa_{\mathbf{t}}$ decision trees, as described in Subsection II-D and illustrated in Fig. 4, when used as a classifier. Additionally, we compare its efficacy against three other established methods for Wi-Fi sensing, namely: 1) STFT-based feature extraction combined with a CNN classifier [26], 2) an SVM-based classifier, and 3) a DNN-based classifier. These represent state-of-the-art Wi-Fi sensing methods widely used in occupancy and activity detection tasks, and are now referred to as benchmarks. For the SVM and DNN classifiers, we utilize the features from Feature Set Ξ, as outlined in Subsection II-D and Fig. 4.

A. Configuring Parameters for Feature Extraction, Training and Testing Dataset

In each measurement trial, four CSI amplitude datasets were acquired, corresponding to four distinct transmitter-receiver (Tx-Rx) links. Each dataset comprised 15,000 CSI amplitudes, with each CSI amplitude representing an acquisition of the complex S_{21}'s amplitude. The first 12,000 CSI amplitudes were utilized to extract features for training datasets, while the remaining 3,000 CSI amplitudes were used for feature extraction in testing datasets. The CSI amplitude window and feature window had sizes of $N_{\mathrm{C}} = 100$ and $N_{\mathrm{F}} = 8$, respectively. Additionally, the step size for the CSI amplitude window was set to $N_{\mathrm{s}} = 30$.

After feature extraction, the training and testing dataset included 2,400 and 600 data samples per classification category, respectively. The classifier was tasked with determining whether the area of interest was occupied or unoccupied. Each data sample in the training or testing dataset was defined by a set of features. The training and testing of the algorithms was conducted on a workstation which featured an AMD Ryzen 9 7940HX processor with 32 GB of RAM. Feature extraction was carried out in MATLAB, while the machine learning algorithm was trained and tested using Python.

B. Statistical Analysis of the Channel Parameters

Table III provides statistics for extracted channel parameters from different scenarios (AP Position I and AP Position II as shown in Fig. 7) and communication links (A, B, C, D). These channel parameters were used to characterize the behavior of channels in the office environment. The median values for parameters like δ^2 and K help to understand the channel behavior in each scenario. For instance, higher median K values represent environments with a stronger LoS component, while lower median values indicate a decrease in the LoS signal power, an increase in the scattered multipath contribution, or a combination of both. The IQR provides insight into the variability of the observed features. Scenarios with high IQR, such as AP Position II Link A, indicate more variability, which can imply frequent changes in the environment, such as people moving. The K-factor helps distinguish between the dominance of a LoS path and scattered multipath. Higher K values, such as those observed in AP Position II Link C, represent stronger LoS components, which are generally favorable for high data rates. The mean, standard deviation (STD), and PAR provide additional insights into the power-related parameters.

For AP Position I, Link A displays high stability with a strong median dominant component ($\delta^2 = 0.9943$). Link B shows a slightly lower median value for δ^2 (0.9824), suggesting that the walking person may have disturbed this link more compared to the other links. In Links A and C, the higher values of K (175.3 and 157.9, respectively) indicate the presence of a particularly strong LoS component. For AP Position II, in general, the IQR values for K are higher compared to AP Position I, especially Link C, indicating greater variability in the channel conditions (as shown in Fig. 8, channel conditions of Link C change significantly). Notably,

TABLE II: Areas where three participants were located in each scenario

Occupancy Settings	1	2	3	4	5	6	7	8
Located Areas	1, 2, 3	2, 3, 4	3, 4, 5	4, 5, 6	5, 6, 7	6, 7, 8	7, 8, 1	8, 1, 2

TABLE III: Statistics of some important extracted features

AP Position	**Link**	**Statistics**	**Parameters/Features**				
			δ^2	K	**Mean**	**STD**	**PAR**
AP Position I	A	Median	0.9943	175.3	0.9986	0.0535	1.2599
		IQR	0.0045	135.1	0.0011	0.0205	0.1156
	B	Median	0.9824	55.9	0.9956	0.0940	1.4743
		IQR	0.0158	51.9	0.0039	0.0411	0.2455
	C	Median	0.9937	157.9	0.9984	0.0563	1.2764
		IQR	0.0051	123.3	0.0013	0.0220	0.1261
	D	Median	0.9867	74.2	0.9967	0.0818	1.4102
		IQR	0.0116	67.3	0.0029	0.0349	0.1980
AP Position II	A	Median	0.9919	122.7	0.9980	0.0638	1.3065
		IQR	0.0297	216.5	0.0074	0.0847	0.4077
	B	Median	0.9868	75.0	0.9967	0.0814	1.4025
		IQR	0.0935	273.3	0.0230	0.1760	0.9530
	C	Median	0.9959	245.2	0.9990	0.0453	1.2167
		IQR	0.0201	671.0	0.0050	0.0774	0.3868
	D	Median	0.9959	244.5	0.9990	0.0453	1.2154
		IQR	0.0059	385.1	0.0015	0.0316	0.1608

TABLE IV: Comparison with DNN, CNN, and SVM-based Methods: Averaged Evaluation Metrics Across All Office Areas Based on the closest Tx-Rx link (Precision, Recall, and F1-score Calculated for the Occupied Class)

Method	**Accuracy**	**Precision**	**Recall**	**F1-Score**	**Feature Extraction + Testing Time (s)**
Top $\kappa_{\mathbf{t}}$ decision trees	0.9828	0.9819	0.9839	0.9828	0.1058
Feature Set Ξ + SVM	0.6009	0.6148	0.5761	0.5840	0.2132
Feature Set Ξ + DNN	0.5919	0.6069	0.5214	0.5454	0.2840
STFT + CNN	0.6238	0.2324	0.3041	0.2302	0.2955

Link C and D has an exceptionally high median K value (245.2), indicating a very dominant signal path. The PAR value is also higher for AP Position II, suggesting greater peak-to-average power ratios, which could impact signal quality during fading conditions.

In summary, AP Position I appears to have more consistent communication characteristics with generally lower IQR values, while AP Position II is subject to higher variability, suggesting more dynamic or challenging propagation conditions.

C. Evaluation of Office Occupancy Based on Only One Tx-Rx Link

The performance of four occupancy detection methods at the eight desks is illustrated in Fig. 9. For each desk, only the closest Tx-Rx link is utilized for feature extraction. Specifically, Tx-Rx link A, shown in Fig. 7, is used for desks 1 and 2; Tx-Rx link B is associated with desks 3 and 4; Tx-Rx link C with desks 5 and 6; and Tx-Rx link D with desks 7 and 8. Fig. 9 illustrates that the top $\kappa_{\mathbf{t}} = 15$ decision trees from $\kappa_{\mathrm{a}} = 1800$ decision trees have the highest accuracy compared to the other methods, while STFT-based feature extraction combined with a CNN classifier ("STFT, CNN")[2], SVM-based classifier and DNN-based classifier with Feature Set Ξ ("Feature Set Ξ, SVM" and "Feature Set Ξ, DNN")[3] exhibit similar trends with intermediate accuracy levels.

As the training phase is performed offline, we focus on the execution time of the online classification phase[4]. Table IV presents a comparative evaluation of the different methods in terms of average accuracy, and the time for the online classification phase, i.e., the combined feature extraction and testing time. In Table IV, the "Top $\kappa_{\mathbf{t}}$ decision trees" method demonstrates the highest average accuracy at 0.9828, outperforming other methods such as SVM (0.6467), DNN (0.6300), and CNN (0.6481). Importantly, the system's effectiveness in practical deployment is primarily influenced by how efficiently it can extract features and provide predictions. For real-world

[2]The CNN architecture considered in this paper starts with an input layer, followed by three convolutional blocks. Each block consists of a convolutional layer with filters of size 16, 32, and 64, respectively, all using "relu" activation and "same" padding, followed by 2×2 max pooling, batch normalization, and a dropout layer for regularization (0.25 rate). After the convolutional blocks, the model flattens the output and passes it through a dense layer with 128 units ("relu" activation), followed by a 0.5 dropout layer. Finally, the model ends with a softmax output layer, classifying into the specified number of classes.

[3]The DNN-based classifier features a first dense layer with 128 "relu" units, followed by a 0.5 dropout layer to mitigate overfitting. It then includes another dense layer with 64 "relu" units, followed by another 0.5 dropout layer. The model concludes with a softmax layer that classifies into two categories: occupied and unoccupied.

[4]The training process is a one-time task that can be performed offline. As a result, a long training time does not impact the real-time performance of the proposed approach.

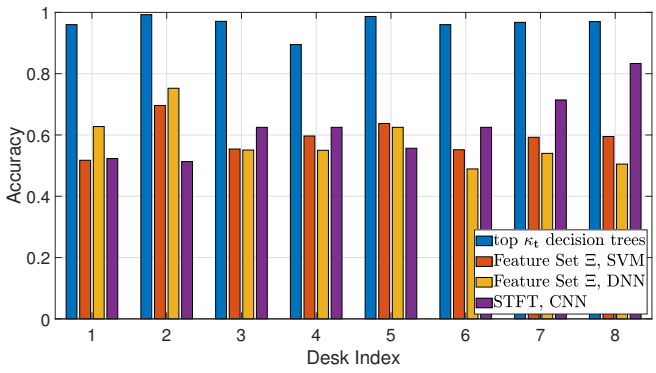

(a)

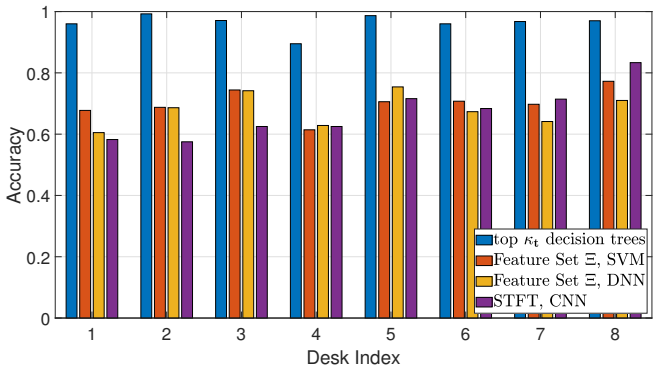

(b)

Fig. 9: The accuracy of different methods for detecting office occupancy based on only the closest Tx-Rx link: (a) the transmitter antenna is located at the center of the office room; (b) the transmitter antenna is located near one of the wall.

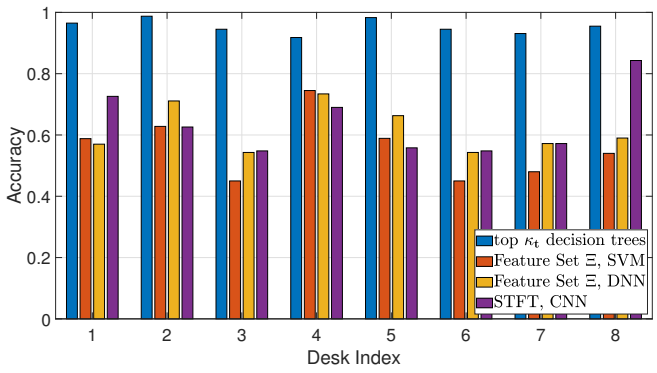

(a)

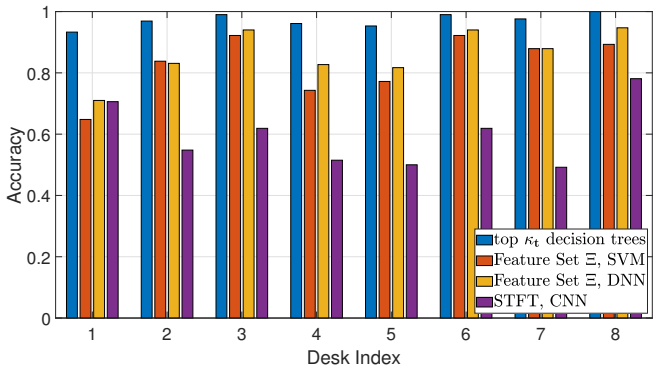

(b)

Fig. 10: The accuracy of different methods for detecting office occupancy based on all Tx-Rx links: (a) the transmitter antenna is located at the center of the office room; (b) the transmitter antenna is located near one of the wall.

applications, rapid feature extraction and testing ensure that the system can deliver reliable results with minimal delay, which is essential for low latency (near real-time) applications. The "Top κ_t decision trees" method has the lowest combined feature extraction and testing time of 0.1058 seconds. In comparison, the SVM, DNN and STFT,CNN methods require longer times, 0.2132 seconds, 0.2840 seconds and 0.2955 seconds, respectively. In this comparison, it is evident that the low feature extraction and testing time for "Top κ_t decision trees", coupled with superior accuracy, makes it highly suitable for real-time applications.

In addition to accuracy and runtime, we evaluated each method using standard classification metrics including precision, recall, and F1-score. These metrics provide a more comprehensive view of classifier performance, particularly in scenarios with varying occupancy dynamics. As shown in Table IV, the proposed method achieves the highest F1-score (0.98), indicating a strong balance between precision and recall. Comparatively, the benchmark methods (SVM, DNN, and STFT+CNN) exhibit lower scores, highlighting the superior performance and robustness of our approach.

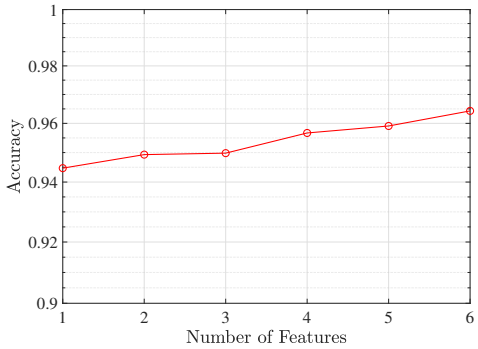

Fig. 11: Effect of Number of Top Features on Model Accuracy.

D. Minimum Feature Set Analysis for 90% Accuracy

To evaluate the minimum number of features required to maintain high classification performance, we conducted an iterative feature selection experiment based on random forest importance ranking. Starting from the highest-ranked feature, we progressively added features one by one and recorded the corresponding classification accuracy.

As illustrated in Fig. 11, the system achieves an accuracy above 90% using only the most important feature, which corresponds to the CCT extracted under a specific threshold.

TABLE V: Ablation Study Evaluating the Impact of Channel Model-based Features and the Feature Selection Process: Averaged Evaluation Metrics Across All Office Areas Based on the closest Tx-Rx link (Precision, Recall, and F1-score Calculated for the Occupied Class)

Method	Accuracy	Precision	Recall	F1-Score
Proposed Method	0.9828	0.9819	0.9839	0.9828
No Channel Model-based Features	0.6525	0.6492	0.6594	0.6535
No Feature Selection	0.8456	0.8866	0.7970	0.8361

As more top-ranked features are added, accuracy continues to improve, reaching over 96% with just six features. This indicates that a compact subset of physically meaningful features can effectively capture occupancy-related channel variations, enabling low complexity and interpretable classification.

This result highlights the efficiency of our channel model-based feature engineering pipeline and the potential for dimensionality reduction in resource-constrained or real-time applications.

E. Ablation Study and Standard Metrics Evaluation

To further validate the effectiveness of each component in our proposed method, we conducted an ablation study by selectively disabling the channel model-based features and the feature selection process. Table V summarizes the average classification performance across all office areas, focusing on the occupied class as the positive class. The evaluation includes Accuracy, Precision, Recall, and F1-score. As shown, removing the channel model-based features leads to a significant drop in performance (e.g., the F1-score reduces from 0.9828 to 0.6535), indicating the importance of physically interpretable features and temporal modeling. Disabling feature selection also degrades performance, although less severely, suggesting that it improves both classification quality and computational efficiency by removing redundant features.

F. Evaluation of Office Occupancy Based on All Tx-Rx Links

Fig. 10 presents the performance of the four different occupancy detection methods evaluated across eight desks, utilizing all four Tx-Rx links[5]. Notably, an increase in the number of features does not necessarily lead to improved accuracy; in some cases, accuracy slightly decreases. In Fig. 10, the classifier utilizing the top $\kappa_{\mathbf{t}}$ decision trees consistently achieves the highest accuracy in comparison to the other methods. Conversely, the method combining STFT-based feature extraction with a CNN classifier ("STFT, CNN") demonstrates the lowest accuracy across most desk indices. The SVM-based classifier and the DNN-based classifier using Feature Set Ξ ("Feature Set Ξ, SVM" and "Feature Set Ξ, DNN") exhibit comparable performance trends, with accuracy levels falling between those of the other methods.

[5]For a data sample in training or testing dataset, if the total number of features extracted from one Tx-Rx link was 320, when considering four Tx-Rx links, the total number of features was 320 × 4 = 1280. For STFT with a CNN classifier, when a single Tx-Rx link is utilized, the dimensions of STFT image matrix is 32×19. When considering four Tx-Rx links, the dimensions of the STFT image matrix expanded to $32 \times (19 \times 4) = 32 \times 76$.

Experimental results demonstrate that our channel parameter-based approach at 6 GHz significantly outperforms traditional methods, achieving higher accuracy with substantially lower computational overhead. Such clear advantages underline the effectiveness and practicality of selecting 6 GHz band and utilizing physically-interpretable channel parameters for occupancy detection.

G. Analysis of Real-World Deployment Factors

Hardware variability: Although hardware diversity can lead to variations in CSI measurements due to differences in sampling resolution, quantization, and internal calibration, our system exclusively uses amplitude-based, window-aggregated features (such as Rician K-factor, coherence time, and AFD). These features are statistical in nature and depend on signal fluctuation patterns rather than raw phase alignment, making them robust to many hardware-specific artifacts. While a detailed evaluation of cross-device generalization is beyond the scope of this study, we identify this as a valuable direction for future work, particularly in federated learning or domain adaptation contexts.

Channel Frequency Considerations and Path Loss Mitigation: Although the 6 GHz band offers higher spatial resolution and reduced interference, it is also associated with increased free-space path loss compared to 2.4 and 5 GHz bands (for example the additional path loss at 6.4 GHz compared to 5 GHz at 10 m is approximately 2.1 dB). In this work, we address this limitation in three ways. First, the system is deployed in a short-range indoor environment with typical AP-to-STA distances under 10 meters, often with clear LoS conditions. Second, we employ ceiling-mounted placement to maximize signal coverage and SNR. Third, the extracted features—such as the Rician K-factor, CCT, and AFD—are statistical in nature and rely on temporal and spatial variation patterns rather than absolute signal power, which enhances robustness under low-SNR conditions.

Comparison to prior work: Our method targets real-time occupancy detection using physically interpretable, channel-model-based features and compact classifiers. Deep models (e.g., STFT+CNN, deep DNNs) often achieve high accuracy but typically assume richer hardware and larger compute/label budgets. In contrast, our features facilitate millisecond-level inference. The design emphasizes model transparency rather than pursuing incremental gains in peak accuracy; while more computationally intensive models can raise the upper-bound, they do so at substantially higher cost and complexity.

V. Conclusion

This study demonstrates the potential of leveraging 6 GHz Wi-Fi sensing for real-time office occupancy detection. By integrating physically interpretable, channel model-based features with a random forest classifier, we developed a low-complexity and highly accurate system. Real-world measurements in a sub-7 GHz office environment, aligned with IEEE 802.11 standards, provided insight into the wireless channel behavior. The proposed method achieves an average accuracy of 98.28% with a total inference time of only 0.1058 seconds, significantly outperforming baseline approaches in both accuracy and efficiency. These results affirm the feasibility of deploying our approach in live smart office systems for applications such as energy optimization, security monitoring, and adaptive workspace management.

Future work will investigate the generalization of CSI-based features across heterogeneous Wi-Fi hardware using cross-device training and domain adaptation. We also plan to assess the system's robustness under real-world interference and explore adaptive sensing strategies for dynamic or dense environments. Extending the framework to support online learning and multimodal sensing (e.g., combining Wi-Fi with vision or acoustic data) may further enhance adaptability and behavioral insight.

References

[1] J. Zhang, Y. Li, H. Xiong, D. Dou, C. Miao and D. Zhang, "HandGest: Hierarchical Sensing for Robust-in-the-Air Handwriting Recognition With Commodity WiFi Devices," *IEEE Internet Things J.*, vol. 9, no. 19, pp. 19529-19544, 1 Oct.1, 2022.

[2] H. Li, K. Ota, M. Dong and M. Guo, "Learning Human Activities through Wi-Fi Channel State Information with Multiple Access Points," *IEEE Commun. Mag.*, vol. 56, no. 5, pp. 124-129, May 2018.

[3] Z. Wang, B. Guo, Z. Yu and X. Zhou, "Wi-Fi CSI amplitudes-Based Behavior Recognition: From Signals and Actions to Activities," *IEEE Commun. Mag.*, vol. 56, no. 5, pp. 109-115, May 2018.

[4] L. Chen, X. Chen, L. Ni, Y. Peng and D. Fang, "Human Behavior Recognition Using Wi-Fi CSI amplitudes: Challenges and Opportunities," *IEEE Commun. Mag.*, vol. 55, no. 10, pp. 112-117, Oct. 2017.

[5] "IEEE Draft Standard for Information Technology – Telecommunications and Information Exchange Between Systems Local and Metropolitan Area Networks – Specific Requirements - Part 11: Wireless LAN Medium Access Control (MAC) and Physical Layer (PHY) Specifications-Amendment 4: Enhancements for Wireless Local Area Network (WLAN) Sensing," *IEEE P802.11bf/D4.0, April 2024*, vol., no., pp.1-231, 22 Apr. 2024.

[6] R. Du et al., "An Overview on IEEE 802.11bf: WLAN Sensing," *IEEE Commun. Surv. Tutorials.*, vol. 27, no. 1, pp. 184-217, Feb. 2025.

[7] F. Meneghello, A. Blanco, A. Cusano, J. Widmer and M. Rossi, "Wi-Fi Multi-Path Parameter Estimation for Sub-7 GHz Sensing: A Comparative Study," *2023 19th International Conference on Wireless and Mobile Computing, Networking and Communications (WiMob)*, Montreal, QC, Canada, pp. 237-242, 2023.

[8] F. Meneghello, C. Chen, C. Cordeiro and F. Restuccia, "Toward Integrated Sensing and Communications in IEEE 802.11bf Wi-Fi Networks," *IEEE Commun. Mag.*, vol. 61, no. 7, pp. 128-133, July 2023.

[9] C. Chen, H. Song, Q. Li, F. Meneghello, F. Restuccia and C. Cordeiro, "Wi-Fi Sensing Based on IEEE 802.11bf," *IEEE Commun. Mag.*, vol. 61, no. 1, pp. 121-127, Jan. 2023.

[10] A. Zhuravchak, O. Kapshii, and E. Pournaras, "Human activity recognition based on wi-fi CSI amplitudes data-a deep neural network approach," *Procedia Comput. Sci.* 198, 59–66, 2022.

[11] G. Lin, W. Jiang, S. Xu, X. Zhou, X. Guo, Y. Zhu, "Human Activity Recognition Using Smartphones With WiFi Signals," *IEEE Trans. Hum. Mach. Syst.*, vol. 53, no. 1, pp. 142-153, Feb. 2023.

[12] R. C. Chen, C. Dewi, S. W. Huang, and R. Caraka, "Selecting Critical Features for Data Classification Based on Machine Learning Methods," *J. Big Data*, vol. 7, p. 52, 2020.

[13] J. Ding, Y. Wang, H. Si, S. Gao and J. Xing, "Three-Dimensional Indoor Localization and Tracking for Mobile Target Based on WiFi Sensing," *IEEE Internet Things J.*, vol. 9, no. 21, pp. 21687-21701, Nov. 2022.

[14] G. Y. Tao and L. Zhao, "Fingerprint localization with adaptive area search," *IEEE Commun. Lett.*, vol. 24, no. 7, pp. 1446–1450, Jul. 2020.

[15] Y. Zhang, D. Li, and Y. Wang, "An indoor passive positioning method using CSI fingerprint based on adaboost," *IEEE Sensors J.*, vol. 19,no. 14, pp. 5792–5800, Jul. 2019.

[16] Y. Zhang, C. Wu, and Y. Chen, "A low-overhead indoor positioning system using CSI fingerprint based on transfer learning," *IEEE Sensors J.*, vol. 21, no. 16, pp. 18156–18165, Aug. 2021.

[17] X. Wang, X. Wang, and S. Mao, "Indoor fingerprinting with bimodal CSI tensors: A deep residual sharing learning approach," *IEEE Internet Things J.*, vol. 8, no. 6, pp. 4498–4513, Mar. 2021.

[18] W. Wang, A. X. Liu, M. Shahzad, K. Ling and S. Lu, "Device-Free Human Activity Recognition Using Commercial WiFi Devices," *IEEE J. Sel. Areas Commun.*, vol. 35, no. 5, pp. 1118-1131, May 2017.

[19] J. Yang, H. Zou, H. Jiang and L. Xie, "Device-Free Occupant Activity Sensing Using WiFi-Enabled IoT Devices for Smart Homes," *IEEE Internet Things J.*, vol. 5, no. 5, pp. 3991-4002, Oct. 2018.

[20] W. Liu, S. Chang, Y. Liu, and H. Zhang, "Wi-PSG: Detecting rhythmic movement disorder using COTS WiFi," *IEEE Internet Things J.*, vol. 8,no. 6, pp. 4681–4696, Mar. 2021.

[21] M. Salman, Y.-D. Soe, and Y. Noh, "WiFi-enabled occupancy monitoring in smart buildings with a self-adaptive mechanism," *Proc. 38th ACM/SIGAPP Symp. Appl. Comput. (SAC)*, Tallinn, Estonia, Mar. 2023, pp. 759–762.

[22] M. Salman, L. A. Caceres-Najarro, Y.-D. Seo, and Y. Noh, "WiSOM: WiFi-enabled self-adaptive system for monitoring the occupancy in smart buildings," *Energy*, vol. 294, Art. no. 130420, 2024.

[23] O. Zeleny, T. Fryza, T. Bravenec, S. Azizi, and G. Nair, "Detection of room occupancy in smart buildings," *Radioengineering*, vol. 33, no. 3, pp. 432–441, Sept. 2024.

[24] Y. He, Y. Chen, Y. Hu, and B. Zeng, "WiFi vision: Sensing, recognition, and detection with commodity MIMO-OFDM WiFi," *IEEE Internet Things J.*, vol. 7, no. 9, pp. 8296–8317, Sep. 2020.

[25] J. Zhang et al., "Data augmentation and dense-LSTM for human activity recognition using WiFi signal," *IEEE Internet Things J.*, vol. 8, no. 6,pp. 4628–4641, Mar. 2021.

[26] H. Lee, C. R. Ahn, and N. Choi, "Fine-grained occupant activity monitoring with Wi-Fi channel state information: Practical implementation of multiple receiver settings," *Adv. Eng. Inform.*, vol. 46, Art. no. 101147, Oct. 2020.

[27] S. Kianoush, S. Savazzi, and V. Rampa, "Leveraging MIMO-OFDM Radio Signals for Device-Free Occupancy Inference: System Design and Experiments," *EURASIP J. Adv. Signal Process.*, vol. 2018, no. 44, 2018.

[28] H. E. Zein, F. Mourad-Chehade, and H. Amoud, "Leveraging Wi-Fi CSI amplitudes Data for Fall Detection: A Deep Learning Approach," in *2023 5th International Conference on Bio-engineering for Smart Technologies (BioSMART)*, Paris, France, 2023, pp. 1-4.

[29] B. Yu, Y. Wang, K. Niu, Y. Zeng, T. Gu, L. Wang, C. Guan, and D. Zhang, "WiFi-Sleep: Sleep Stage Monitoring Using Commodity Wi-Fi Devices," *IEEE Internet Things J.*, vol. 8, no. 18, pp. 13900-13913, Sept. 2021.

[30] H. Wang, D. Zhang, Y. Wang, J. Ma, Y. Wang, and S. Li, "RT-Fall:A real-time and contactless fall detection system with commodity Wi-Fi devices," *IEEE Trans. Mobile Comput.*, vol. 16, no. 2, pp. 511–526,Feb. 2017.

[31] W. Qi, R. Zhang, J. Zhou, H. Zhang, Y. Xie, and X. Jing, "A Resource-Efficient Cross-Domain Sensing Method for Device-Free Gesture Recognition With Federated Transfer Learning," *IEEE Trans. Green Commun. Netw.*, vol. 7, no. 1, pp. 393-400, Mar. 2023.

[32] D. Wang, J. Yang, W. Cui, L. Xie and S. Sun, "AirFi: Empowering WiFi-Based Passive Human Gesture Recognition to Unseen Environment via Domain Generalization," *IEEE Trans. Mob. Comput.*, vol. 23, no. 2, pp. 1156-1168, Feb. 2024.

[33] J. Yang, H. Zou and L. Xie, "SecureSense: Defending Adversarial Attack for Secure Device-Free Human Activity Recognition," *IEEE Trans. Mob. Comput.*, vol. 23, no. 1, pp. 823-834, Jan. 2024.

[34] "IEEE Draft Standard for Information technology–Telecommunications and information exchange between systems Local and metropolitan area networks–Specific requirements - Part 11: Wireless LAN Medium Access Control (MAC) and Physical Layer (PHY) Specifications Amendment: Enhancements for Extremely High Throughput (EHT)," *IEEE P802.11be/D7.0, August 2024*, vol., no., pp.1-1089, 1 Aug. 2024.

[35] L. Galati-Giordano, G. Geraci, M. Carrascosa and B. Bellalta, "What will Wi-Fi 8 Be? A Primer on IEEE 802.11bn Ultra High Reliability," *IEEE Commun. Mag.*, vol. 62, no. 8, pp. 126-132, Aug. 2024.
[36] L. J. Greenstein, D. G. Michelson and V. Erceg, "Moment-method estimation of the Ricean K-factor," *IEEE Commun. Lett.*, vol. 3, no. 6, pp. 175-176, June 1999.
[37] A. Abdi, C. Tepedelenlioglu, M. Kaveh and G. Giannakis, "On the estimation of the K parameter for the Rice fading distribution," *IEEE Commun. Lett.*, vol. 5, no. 3, pp. 92-94, Mar. 2001.
[38] M. O. Hasna and M. . -S. Alouini, "Outage probability of multihop transmission over Nakagami fading channels," *IEEE Commun. Lett.*, vol. 7, no. 5, pp. 216-218, May 2003.
[39] G. K. Karagiannidis, T. A. Tsiftsis and R. K. Mallik, "Bounds for multihop relayed communications in Nakagami-m fading," *IEEE Trans. Commun.*, vol. 54, no. 1, pp. 18-22, Jan. 2006.
[40] R. K. Mallik, "A New Statistical Model of the Complex Nakagami-m Fading Gain," *IEEE Trans. Commun.*, vol. 58, no. 9, pp. 2611-2620, September 2010.
[41] M. Yacoub, "The κ-μ distribution and the η-μ distribution," *IEEE Antennas Propag. Mag.*, vol. 49, no. 1, pp. 68–81, Feb. 2007.
[42] S. K. Yoo et al., "The κ-μ / Inverse Gamma and η-μ / Inverse Gamma Composite Fading Models: Fundamental Statistics and Empirical Validation," *IEEE Trans. Commun.*, vol. 69, no. 8, pp. 5514-5530, Aug. 2021.
[43] N. Simmons, C. R. N. D. Silva, S. L. Cotton, P. C. Sofotasios, S. K. Yoo and M. D. Yacoub, "On Shadowing the κ-μ Fading Model," *IEEE Access*, vol. 8, pp. 120513-120536, 2020.
[44] AntennaWare, "BodyWave UWB Antenna," *AntennaWare*. [Online]. Available: https://antennaware.co.uk/product/bodywave/uwb-antenna.